Supporting Information

Tseng et al. 10.1073/pnas.1106377109

SI Methods

siRNA Treatments. Transient silencing was performed using 15 nM siRNA P120-catenin: 5′-AACGAGGUUAUCGCUGAGAAC-3′; GFP: 5′-GACGUAAACGGCCACAAGUUC-3′) and retrotransfection with Lipofectamine 2000 according to the manufacturer's instructions (Invitrogen). Lysates of cells were prepared in RIPA lysis buffer [10 mM Tris·HCl (pH 7.4), 150 mM NaCl, 1% (vol/vol) Triton X-100, 0.1% (vol/vol) SDS, 0.5% (vol/vol) sodium deoxycholate, and 1 mM EDTA] containing a protease and phosphatase inhibitor mixtures (P8340, P2850, P5726; Sigma-Aldrich). Equivalent amounts of protein were processed by SDS/PAGE and transferred to PVDF membrane (Hybond-P; Amersham Biosciences). Immunoblotting was performed using the following primary antibodies: Integrin-β1 and P120-catenin (BD Biosciences) and β-actin (Abcam).

Video Microscopy and Image Acquisition. Time-lapse acquisitions were taken with an inverted microscope (Axiovert 200M; Carl Zeiss). Temperature, CO_2, and humidity control was performed using a Box and Brick System (Life Imaging Services). Multiple positions were recorded using an XY motorized stage (Marzhauser). Nucleus movements were followed with a 15-min time frame and a 10× dry phase-contrast objective over 48 h.

Fluorescent image acquisitions of fixed cells were taken using an upright microscope (BX61; Olympus) with 100× (N.A. 1.4) oil-immersion objectives mounted on a piezo motor (Physics Instruments). Both microscopes were controlled with MetaMorph software (MDS Analytical Technologies).

Averaged images were obtained by aligning multiple images taken on distinct cells and projecting them onto a single image by calculating the average fluorescence intensity of each pixel.

Automated Nucleus Tracking. Micropattern images (taken with a 10× objective) from each stage position were first segmented to 36 subregions corresponding to a 6 × 6 array of micropatterns. Subregions were screened for the existence of a nucleus by standard deviation of pixel intensities. Nucleus images were then convolved by a 9 × 9 "Mexican hat" kernel. Binarized nucleus images were obtained by automatic thresholding and a median filter to remove isolated noise pixels. After "watershed" segmentation, the number of nuclei was determined considering their size and shape factor as well. Only subregions containing only one nucleus at the beginning were selected for subsequent mitosis detection. Based on the nucleus shape factor, intensity variation, and the number of nuclei detected, division from one cell to two cells could be detected. At these positions only, orientations of the nucleus–nucleus axis were recorded after cell division. The measurements continued until the end of the time-lapse series or the detection of the second mitosis event.

Glass Slide Micropatterning. Glass coverslip micropatterning has been described elsewhere (1). Coverslips were first spin-coated with adhesion promoter Ti Prime (MicroChemicals) and then with 0.5% polystyrene in toluene at 3,000 rpm. Polystyrene-coated coverslips were oxidized through oxygen plasma (FEMTO; Diener Electronic) for 10 s at 30 W before incubation with 0.1 mg/mL poly-L-lysine(20)-g[3.5]-poly-ethyleneglycol (PLL-PEG) (Surface Solutions) in 10 mM Hepes (pH 7.4) for 15 min. After drying, coverslips were exposed to deep UV (UVO cleaner; Jelight) through a photomask (Toppan) for 2 min. Right after UV activation, coverslips were incubated with 20 μg/mL fibronectin (Sigma), another selected ECM protein when specifically mentioned (type 1 collagen from rat tail; Sigma), or laminin (Sigma), and 10 μg/mL of fluorescent fibrinogen conjugate (Invitrogen) solution in PBS for 30 min. Coverslips were washed three times with sterile PBS before plating cells.

Polyacrylamide Micropatterning. Micropatterned polyacrylamide gels were made as previously described (2). Briefly, fluorescent beads (dark red 200 nm; F-8807; Invitrogen) were first passivated by PLL-PEG (2) (Surface Solutions). Acrylamide (6.67%) and bis-acrylamide (0.167%) solution, containing the passivated beads, was polymerized between the photomask (Toppan) and acryl-silanized coverslips. The resulting polyacrylamide gel had a thickness of 70 μm and rigidity of 7 kPa. After deep UV activation through the photomask, the gel was incubated with the cross-linker *N*-hydroxysuccinimide (Fluka) and 1-ethyl-3-(3-dimethylaminopropyl)carbodiimide hydrochloride (Pierce) before coating with fibronectin (Sigma) and fluorescent conjugated fibrinogen (Invitrogen).

Physical Modeling and Numerical Simulations. When cells spread on a patterned substrate, they optimize their shape by minimizing energy. This simple argument has been demonstrated in the case of single cells and a lattice of adhesive proteins. The extension of this argument to the case of two cells is the purpose of this material.

We suppose that the energy of the cell doublet can be separated into three parts as in the equation

$$H = H_1 + H_2 + H_{12},$$

where H_1 and H_2 are the self-energy, respectively, of cell 1 and of cell 2 within the doublet. The coupling term H_{12} accounts for the interaction energy between cell 1 and cell 2. In our model, cells are considered as 2D homogeneous material. The self-energy terms include (*i*) an adhesion term, corresponding to the energy gain upon binding of integrins with ECM, (*ii*) a line energy term mimicking the energy cost of the tension generated by the actomyosin contractility, and (*iii*) a compressibility term that fixes the mean cell area and allocates an energy cost to variations of cell area. These terms have been thoroughly discussed in the framework of the cellular Potts model in refs. 3–6. To further simplify the analysis, we suppose that first, cell shapes adopt the convex envelope of the micropattern, second, cells have equal areas in the doublet, third, the interfaces are straight, and fourth, this interface passes through the center of the pattern. With these simplifications, terms (*i*) and (*iii*) in the self-energy of cells can be dropped.

The interaction energy H_{12} is written as

$$H_{12} = J_{cell-cell} . L_{cell-cell},$$

where $J_{cell\text{-}cell}$ measures the strength of the cadherin–cadherin interaction and $L_{cell\text{-}cell}$ is the length of the interface between cell 1 and cell 2. Dropping all of the constant terms, the self-energy of cell i = 1,2 is expressed as

$$H_i = \sum_k J_K . L_k,$$

where k is the interface type, L_k is the interface length, and J_k is the line tension of the interface. According to the experimental measurements of the forces (Fig. 5 and Fig. S7), the interfaces have been classified into four types:

k = intra-noECM; corresponds to the type of interface linking integrins to integrins and standing above nonadhesive regions;
k = inter-noECM; corresponds to the type of interface linking integrins and cadherin above nonadhesive regions;
k = intra-ECM; corresponds to the type of interface linking integrins to integrins and standing above adhesive regions;
k = inter-ECM; corresponds to the type of interface linking integrins and cadherin above adhesive regions.

The total energy of the doublet depends then on a set of parameters describing the cell states and on a single variable that defines the orientation of the interface. Our computation will consider various ECM patterns, and we will identify the energy minima as a function of the doublet configuration described by a unique variable. We compare the computations on various patterns with experimental observations. At first we ignore the role of ECM and set all of the cortical line energy equal, that is,

$$J_{intra-noECM} = J_{intra-ECM} = J_{inter-noECM} = J_{inter-ECM} = 1.$$

We also set a value for the cadherin–cadherin interface line energy. Because this interface fluctuates more than the others, the line energy must be smaller and we arbitrarily fixed it to 10% of $J_{intra\text{-}ECM}$. The energy was plotted as a function of the doublet orientation for various types of patterns. Because the cortical line energies are all equal, the self-energy is a constant and is proportional to the perimeter of the doublet. Thus, the variation of the doublet energy is determined only by the changes in intercellular junction length. The energy profile is also independent of the pattern, because they have by construction all of the same perimeters. Considering isotropic line tension is not sufficient to find all of the equilibrium positions of the doublets on the patterns, except in the case of the [square]-shaped micropattern (Fig. S7). Next, we consider anisotropic cortical energy in response to the presence of ECM and fix the values of the line energies in the same ratio as the force measurements:

$$J_{intra-noECM} = 1.3, J_{inter-noECM} = 0.8, \text{and } J_{intra-ECM} = J_{inter-ECM} = 1.$$

We kept $J_{cell\text{-}cell} = 0.1$. The energy plots are represented in Fig. S7. For clarity, all of the profiles have been shifted by a constant value. In the case of anisotropic cortical tensions, the positions of the energy minima vary from pattern to pattern and systematically correspond to the orientations observed experimentally.

1. Azioune A, Carpi N, Tseng Q, Théry M, Piel M (2010) Protein micropatterns: A direct printing protocol using deep UVs. *Methods Cell Biol* 97:133–146.
2. Tseng Q, et al. (2011) A new micropatterning method of soft substrates reveals that different tumorigenic signals can promote or reduce cell contraction levels. *Lab Chip* 11:2231–2240.
3. Käfer J, Hayashi T, Marée AF, Carthew RW, Graner F (2007) Cell adhesion and cortex contractility determine cell patterning in the *Drosophila* retina. *Proc Natl Acad Sci USA* 104:18549–18554.
4. Vianay B, et al. (2010) Single cells spreading on a protein lattice adopt an energy minimizing shape. *Phys Rev Lett* 105:128101.
5. Farhadifar R, Röper JC, Aigouy B, Eaton S, Jülicher F (2007) The influence of cell mechanics, cell-cell interactions, and proliferation on epithelial packing. *Curr Biol* 17: 2095–2104.
6. Rauzi M, Verant P, Lecuit T, Lenne PF (2008) Nature and anisotropy of cortical forces orienting *Drosophila* tissue morphogenesis. *Nat Cell Biol* 10:1401–1410.

Fig. S1. Automated analysis of cell positions and movements. (*A*) Automated detection of mitosis events from fluorescent images of nucleus staining with Hoechst in 10× video-microscopy acquisition and a 15-min time frame. Fluorescence intensity increase during metaphase and object separation during anaphase were both used to detect mitosis. Detections of first and subsequent mitosis were then used to determine the part of the movie in which daughter cell positions could be analyzed. (*B*) Example of image thresholding and segmentation to detect nucleus positions and automatically record nucleus–nucleus orientation. (*C*) The measured angles of nucleus–nucleus axis orientation over time (*Upper Left*) from all movies were pooled and plotted together in a circular histogram showing the angular distribution of cell doublets (*Upper Right*). The histogram has been made circular for clarity but is identical modulo 180°. In addition, for each movie, the instantaneous angular speed was calculated at every time point (*Lower Left*). Comparison between measured value and personal visual appreciation of movement led to the determination of an arbitrary threshold of 0.3°/min above which cells were considered as moving. For each movie, this threshold was used to calculate the proportion of moving versus nonmoving frames. All these percentages (one per movie) are graphically represented in a scatterplot graphic (*Lower Right*).

Fig. S1

Fig. S2. Intercellular junctions are stabilized by the absence of ECM at their extremities. Cell positions and movement analysis (Fig. S1) of cells on five different geometries of fibronectin-coated micropatterns (images). The presence of anisotropic adhesive or nonadhesive regions in the central part of the geometry had no effect on junction orientation (first to third rows). The absence of ECM at the extremities of the junction stabilizes the junction (fourth and fifth rows).

Fig. S2

Fig. S3. Cell division orientation is not sufficient to determine daughter cell positioning. The automated detection of mitosis (Fig. S1*A*) was used to measure cell division orientation (nucleus–nucleus orientation during anaphase) on [H] (*Upper*) and [hourglass] (*Lower*). Angular distributions of cell division orientation were only slightly biased by ECM geometry (*Left*) because micropattern size was not adapted to single cells that were moving on the micropatterns (Movie S3). Daughter cells refine their positioning after cell division and finally adopted much more biased orientations (*Right*). These data were duplicated from Fig. 1 to be easily compared with cell division orientation. Cell-doublet orientation appeared to result from an active positioning process of daughter cells rather than oriented cell division.

Fig. S3

Fig. S4. Molecular players implicated in intercellular junction positioning. Panels 1–9: Wild-type daughter cell doublets were plated on fibronectin micropatterns, treated with chemical inhibitors for 6 h, and fixed. Panel 10: Wild-type daughter cell doublets were plated on laminin micropatterns. Panels 11 and 12: siRNA-treated cells were plated on micropatterns and fixed 30 h later. Panel 13: Overlay of all angular distributions of cell–cell junctions to help comparison. Cells were fixed in methanol and immunostained against α-catenin (green) and DNA (Hoechst; blue). Each panel shows the spatial distribution of intercellular junction extremities and the angular distribution of junction orientations (measured as described in Fig. 4*A*) as well as a representative set of images that have been used to perform these measurements. For chemical inhibitors, the panel title indicates the drug target and drug concentration (panels 1–9). For siRNA, the panel title indicates the siRNA target, and bottom images show Western blot quantifications of RNA content with control siRNA (directed against GFP) and the tested siRNA.

Fig. S4

Fig. S5. Comparison between cell–cell forces and inter oriented forces. (*A*) Global traction maps were used to list all traction forces and their positions in the cell. (*B*) Cell–cell force corresponds to the force that opposes traction forces on the substrate (*Left*), whereas inter force represents the sum of all force components that were oriented perpendicular to the intercellular junction (*Right*). (*C*) Inter force, that is, the total traction force component oriented toward the intercellular region, is plotted against the genuine cell–cell force calculated without any consideration of force orientation and spatial distribution. In all cases, the inter oriented forces match the genuine cell–cell force. This was particularly true on [H], where all traction force components toward the intercellular junction contributed to the total cell–cell force.

Fig. S5

Fig. S6. ECM induces opposite effects on intra- and intercellular forces. (*A*) Decomposition of traction forces into intra forces oriented toward intracellular space and inter forces oriented toward the intercellular junction. The role of ECM was tested by comparing intra- and intercellular forces along cell edges with ECM (blue arrows in scheme, blue dots in graphs) or without ECM (red arrows in scheme, red dots in graphs). Intracellular forces were compared between [H] and [X], which provide similar intercellular forces along edges without ECM (*Left*). Intercellular forces were compared between [square] and [H], which provide similar intracellular forces along edges with ECM (*Left*). The experiments were repeated three times. Because gel rigidities vary from one slide to the other, the absolute force value changed slightly but the overall tendencies were reproducible. All these data were combined and are shown in Fig. 6*E*. (*B*) Averaged traction force field on a [C]-shaped micropattern. Magnifications correspond to the white square regions in global maps. Arrows indicate force orientation; color and length both represent local force magnitude in pN. Forces were decomposed into intra- and intercellular forces. Intercellular forces along the adhesive edge were compared with those on the nonadhesive edge. The reduction of intercellular forces due to the absence of ECM, previously observed in distinct cells plated on different micropatterns, was even confirmed within individual cells. All statistical comparisons used Student's *t* tests, $^{**}P < 0.005$, $^{***}P < 0.001$.

Fig. S6

Fig. S7. Modeling of the energetic costs of intercellular junction orientations. Numerical simulations of the model described in Fig. 6 and *SI Methods* were performed for various ECM micropattern geometries (*Center* and *Left*, respectively). Simulations were performed in the case of constant tension (regardless of the presence of ECM) (blue curves) and regulated intra- and intercellular tension in response to the presence or absence of ECM (red curves) as described in Fig. 6. Energies were calculated for all intercellular junction orientations (0° corresponds to horizontal junction orientation). Experimental data are reported (*Right*). These data are reported from Figs. 1–3 where they are shown as rose diagrams except for the data shown in the second row, which were not shown in these figures. In all cases, the most frequent intercellular junction orientations observed experimentally corresponded to the energetic wells obtained with the simulations performed in the case of ECM-dependent tensions. This correlation suggests that the regulation of intra- and intercellular forces by ECM could account for the preferred intercellular junction orientation observed experimentally.

Fig. S7

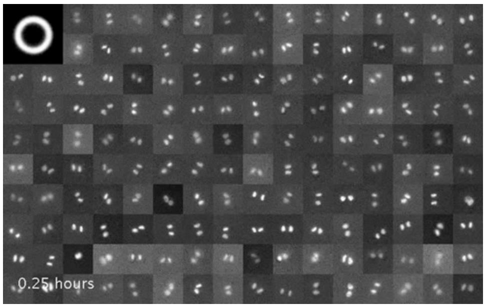

Movie S1. Cell movement on [ring]-shaped micropatterns. Montage of time-lapse movies acquired through a 10× dry objective. Nuclei were stained in living cells with Hoechst 33342 and visualized with epifluorescence microscopy. Images were taken every 15 min.

Movie S1

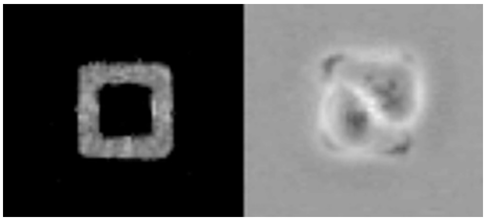

Movie S2. Cell movement on a [square]-shaped micropattern. A [square]-shaped fibronectin micropattern is shown in the left panel. Phase-contrast images during time-lapse acquisition are shown on the right. Daughter cells moved regularly around each other. Images were taken every 15 min.

Movie S2

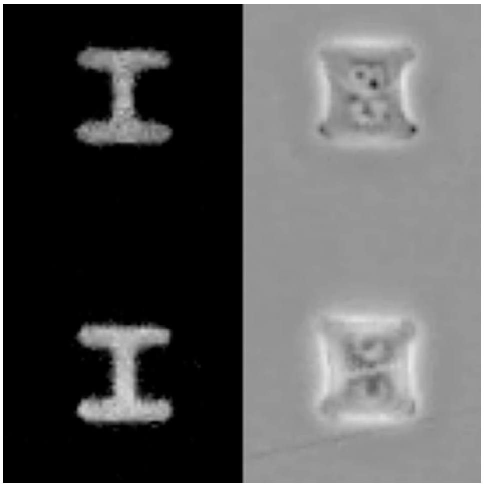

Movie S3. Cell movement on an [H]-shaped micropattern. An [H]-shaped fibronectin micropattern is shown in the left panel. Phase-contrast images during time-lapse acquisition are shown on the right. At the top, cell division is oriented with respect to micropattern geometry, and daughter cells remained positioned according to this orientation. On the bottom, cell division was misoriented but daughter cells corrected their position and adapted it to the micropattern geometry. In both cases, cell positions were maintained steadily until the next division. Images were taken every 15 min.

Movie S3